L-bodies are RNA–protein condensates driving RNA localization in *Xenopus* oocytes

Christopher R. Neil[†,‡], Samantha P. Jeschonek[†,§], Sarah E. Cabral[‡], Liam C. O'Connell, Erin A. Powrie[‖], Jessica P. Otis, Timothy R. Wood[¶], and Kimberly L. Mowry*
Department of Molecular Biology, Cell Biology & Biochemistry, Brown University, Providence, RI 02912

ABSTRACT **Ribonucleoprotein (RNP) granules are membraneless compartments within cells, formed by phase separation, that function as regulatory hubs for diverse biological processes. However, the mechanisms by which RNAs and proteins interact to promote RNP granule structure and function in vivo remain unclear. In *Xenopus laevis* oocytes, maternal mRNAs are localized as large RNPs to the vegetal hemisphere of the developing oocyte, where local translation is critical for proper embryonic patterning. Here we demonstrate that RNPs containing vegetally localized RNAs represent a new class of cytoplasmic RNP granule, termed localization-bodies (L-bodies). We show that L-bodies contain a dynamic protein-containing phase surrounding a nondynamic RNA-containing phase. Our results support a role for RNA as a critical component within these RNP granules and suggest that *cis*-elements within localized mRNAs may drive subcellular RNA localization through control over phase behavior.**

Monitoring Editor
Anita Corbett
Emory University

Received: Mar 26, 2021
Revised: Sep 1, 2021
Accepted: Sep 28, 2021

INTRODUCTION

Spatial organization of the cell cytoplasm has emerged as a key strategy for gene regulation. Indeed, reorganization of otherwise ubiquitously distributed mRNA into specific cytoplasmic foci, termed ribonucleoprotein (RNP) granules, is now recognized as a widespread posttranscriptional regulatory strategy (reviewed in Banani *et al.*, 2017; Shin and Brangwynne, 2017; Gomes and Shorter, 2019; Dodson and Kennedy, 2020). Classes of RNP granules, such as stress granules, P-bodies, neuronal transport granules, and germline specifying granules, have been generally classified by their cellular context and presumed biological function. While physically distinct, these cytoplasmic RNP granules share a striking number of features, including both extensive compositional conservation and potential overlaps in underlying biological function. In addition, emerging research on the physical characteristics of RNP granules may suggest organizational similarities between classes of RNP granules (reviewed in Banani *et al.*, 2017; Gomes and Shorter, 2019).

Phase separation has emerged as a fundamental physical property of RNP granules, offering increased understanding of cellular organization. Multivalent RNA-binding proteins (RBPs) and proteins that contain intrinsically disordered regions (IDRs) are enriched in nearly all known cytoplasmic RNP granule classes (Kedersha *et al*, 2013; Buchan, 2014). Such proteins are thought to work in combination with RNA species that contain multiple protein-binding sites (Han *et al.*, 2012; Kato *et al.*, 2012; Li *et al.*, 2012; Elbaum-Garfinkle *et al.*, 2015; Lin *et al.*, 2015; Nott *et al.*, 2015; Protter *et al.*, 2018) to drive multivalent interactions leading to phase separation (reviewed in Banani *et al.*, 2017; Shin and Brangwynne, 2017; Mittag and Parker, 2018; Gomes and Shorter, 2019). RNP granule components are dispersed in the cytoplasm but can assemble into a condensed liquid or gellike phase to form RNP granules in response to dynamic cues (Hubstenberger *et al.*, 2013; Wang *et al.*, 2014; Han *et al.*, 2018;

This article was published online ahead of print in MBoC in Press (http://www.molbiolcell.org/cgi/doi/10.1091/mbc.E21-03-0146-T) on October 6, 2021.

[†]These authors contributed equally to this work.

The authors declare no competing financial interests.

Present address: [‡]Remix Therapeutics, Cambridge, MA 02139; [§]PerkinElmer Informatics, Waltham, MA 02451; [‖]Olympus Life Science, Waltham, MA 02453; [¶]Avacta Life Sciences, Ltd., Cambridge CB22 4WL, UK.

Author contributions: Conceptualization, C.R.N., S.P.J., K.L.M.; data curation, S.P.J., L.C.O'C.; formal analysis, S.P.J., S.E.C., L.C.O'C., J.P.O.; funding acquisition, K.L.M.; investigation, C.R.N., S.P.J., S.E.C., L.C.O'C., E.A.P., J.P.O., T.R.W.; methodology, C.R.N., S.P.J., S.E.C., L.C.O'C., E.A.P., J.P.O., T.R.W., K.L.M.; software, S.P.J.; supervision, K.L.M.; validation, C.R.N., S.P.J., S.E.C., L.C.O'C., J.P.O.; visualization, C.R.N., S.P.J., S.E.C., L.C.O'C., E.A.P., J.P.O., K.L.M.; writing—original draft, C.R.N., S.P.J., K.L.M.; writing—review and editing, C.R.N., S.P.J., S.E.C., L.C.O'C., E.A.P., J.P.O., K.L.M.

*Address correspondence to: Kimberly L. Mowry (kimberly_mowry@brown.edu).

Abbreviations used: BSA, bovine serum albumin; CRB, column running buffer; FDR, false discovery rate; FRAP, fluorescence recovery after photobleaching; GO, gene ontology; IDR, intrinsically disordered region; IF, immunofluorescence; IP, coimmunoprecipitation; L-bodies, localization-bodies; LC, liquid chromatography; *LE*, localization element; mCh, mCherry; PBS, phosphate-buffered saline; PSM, peptide spectrum match; RBP, RNA-binding protein; RNP, ribonucleoprotein; SE, size exclusion; Stau, Staufen; TBS, Tris-buffered saline.

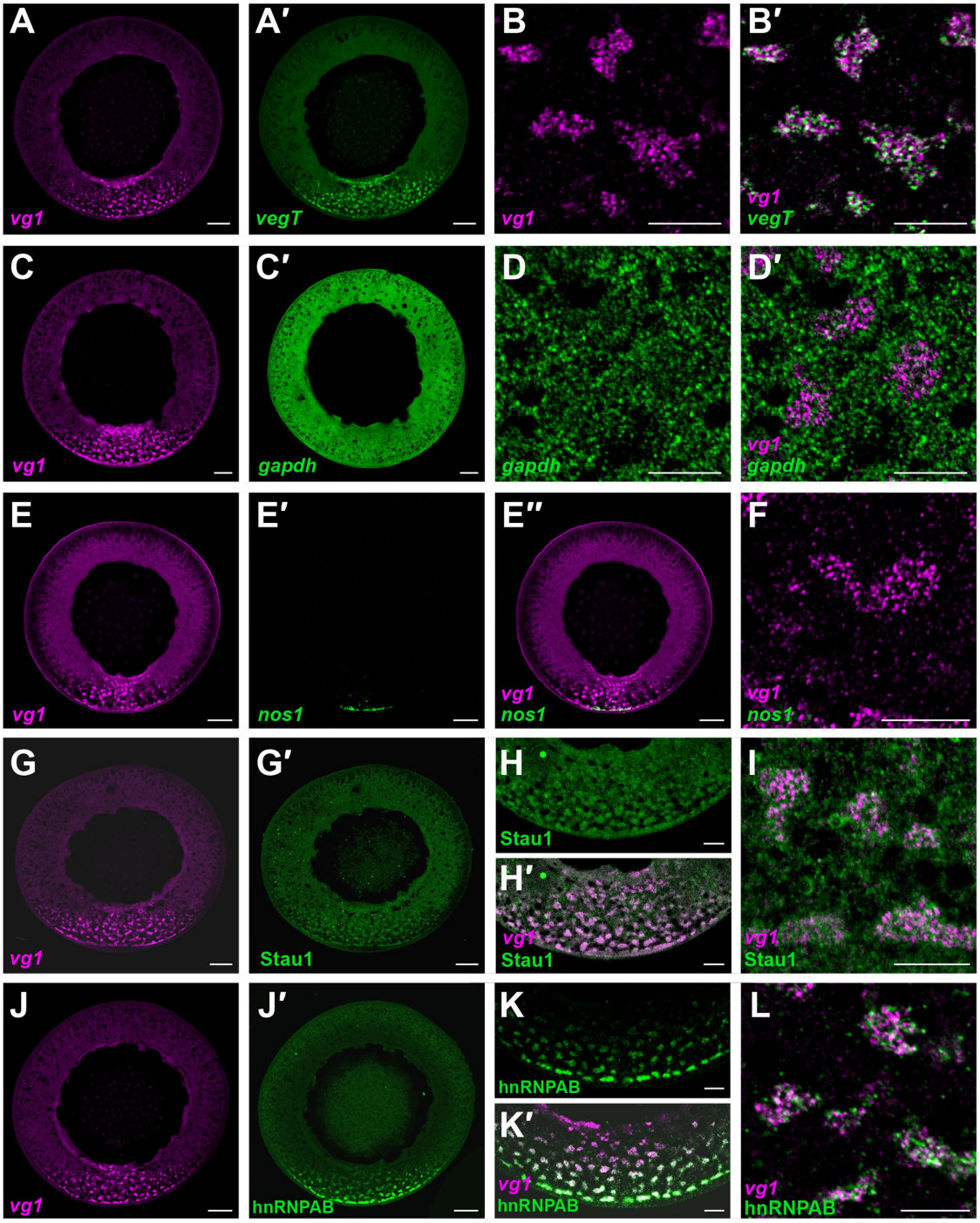

FIGURE 1: Vegetally localizing mRNA is contained in a large RNP complex. (A) A cryosection of a stage II oocyte probed by FISH for *vg1* mRNA (magenta) and *vegT* mRNA (A′, green) is shown, with the vegetal cortex at the bottom. Scale bar = 50 µm. (B) Higher magnification view of the vegetal cytoplasm of a stage II oocyte probed by FISH for *vg1* mRNA (magenta), shown merged in B′ with *vegT* mRNA (green). Scale bar = 10 µm. (C) A cryosection of a stage II oocyte probed by FISH for *vg1* mRNA (magenta) and *gapdh* mRNA (C′, green) is shown, with the vegetal cortex at the bottom. Scale bar = 50 µm. (D) Higher magnification view of *gapdh* mRNA in the vegetal cytoplasm of a stage II oocyte probed by FISH for *gapdh* mRNA (green), shown merged in D′ with *vg1* mRNA (magenta). Scale bar = 10 µm. (E) A cryosection of a stage II oocyte probed by FISH for *vg1* mRNA (magenta) *nos1* mRNA (E′, green), and merged in E″ is shown. The vegetal cortex is at the bottom. Scale bar = 50 µm. (F) Higher magnification view of *nos1* mRNA (green) and *vg1* mRNA (magenta) in the vegetal cytoplasm of a stage II oocyte. The vegetal cortex is at the bottom; scale bar = 10 µm. (G) A cryosection of a stage II oocyte is shown, with the vegetal cortex at the bottom. Combined FISH-IF was used to detect *vg1* mRNA (magenta) and Stau1 protein (G′, green). Scale bar = 50 µm. (H) Combined FISH-IF was used to detect Stau1 (H, green) in the vegetal cytoplasm of a stage II oocyte, merged with *vg1* mRNA (magenta) in H′. Scale bar = 20 µm. (I) High magnification view of the vegetal cytoplasm of a stage II oocyte showing colocalization of *vg1* mRNA (magenta) and Stau1 protein (green). Scale bar = 10 µm. (J) A cryosection of a stage II oocyte is shown with the

Tauber *et al.*, 2020). While it remains an open question how RNAs and proteins determine the physical characteristics of biological condensates, it has become increasingly clear that many RNP granules serve as conserved centers for posttranscriptional gene regulation.

In addition to RNP granule formation, spatial control of mRNA distribution in the cytoplasm is regulated through RNA localization (reviewed in Oh and Houston, 2017; Ryder and Lerit, 2018; Suter, 2018; Holt *et al.*, 2019). RNA localization, which functions to generate cellular polarity in a wide variety of cell types and organisms, proceeds through the binding of *cis*-acting RNA sequences, termed localization elements, and by *trans*-acting protein factors (reviewed in Oh and Houston, 2017; Suter, 2018). In this way, combinations of RNA *cis*-elements and RBPs are required for assembly of specific RNPs that can be localized to distinct regions of the cytoplasm. While certain components of localized RNPs have been identified, the physical nature of these assemblies, and the mechanisms driving their formation, remain largely unknown.

Xenopus laevis oocytes are an important model system for the study of RNA localization. Here, mRNAs encoding germ layer determinants become restricted in the vegetal hemisphere of developing oocytes, where they are subsequently transported to the vegetal cortex and act to pattern the embryo following fertilization (reviewed in Oh and Houston, 2017). mRNAs localized through this pathway, including *vegT* and, most prominently, *vg1* (Weeks and Melton, 1987; Zhang and King, 1996), rely on interactions with a core set of RBPs, including hnRNPAB, PTB, Staufen, and Vera to drive the formation of transport-competent RNP structures (Deshler *et al.*, 1998; Havin *et al.*, 1998; Cote *et al.*, 1999; Yoon and Mowry, 2004; Czaplinski *et al.*, 2005; Czaplinski and Mattaj, 2006; Lewis *et al.*, 2008). Transport of these RNPs to the vegetal cortex is achieved through active transport along microtubules, mediated by kinesin and dynein motor proteins (Betley *et al.*, 2004; Messitt *et al.*, 2008; Gagnon *et al.*, 2013). However, the molecular and physical nature of these and other RNP transport cargos remains uncharacterized.

In this work, we have identified *Xenopus* oocyte transport RNPs, here termed localization-bodies (L-bodies), as novel biomolecular condensates. L-bodies are RNP granules composed of a nondynamic mRNA-containing phase enmeshed in a dynamic protein-containing layer. These large condensates contain a heterogeneous population of localized mRNAs, including *vg1*. Incorporation of mRNAs into L-bodies is correlated with localization and appears to rely on selective enrichment, specified by sequence features of resident mRNAs. Biochemical isolation and proteomic analysis of L-bodies reveals a high degree of compositional similarity to other classes of cytoplasmic RNP granules, with the majority of identified proteins showing either direct conservation with other RNP granule types, or a shared enrichment of multivalent RNA binding domains and IDRs. For the first time, we have characterized the composition and biophysical properties of L-bodies, providing new insights into developmentally programmed localization of maternally loaded mRNAs and the roles that RNP granules play in governing posttranscriptional gene regulation. Importantly, these results suggest a crucial role for mRNA in cytoplasmic granule organization.

RESULTS

L-bodies are large RNP complexes that contain vegetally localizing mRNAs

To characterize the molecular features of RNA transport cargos, we first visualized localized and nonlocalized mRNAs in immature *Xenopus* oocytes by fluorescence in situ hybridization (FISH). During stages II–III of oogenesis, the vegetally localized mRNAs *vg1* and *vegT* are enriched in the vegetal oocyte cytoplasm during localization to the vegetal cortex (Figure 1, A and A′). At higher magnification, *vg1* mRNA foci are restricted to large clusters (Figure 1B), which also contain *vegT* and other localized mRNAs (Figures 1, A′ and B′; Supplemental Figure S1, A and B). These heterotypic vegetal bodies, comprised of multiple RNA foci, are large, ~5–10 µm in size (Figure 1, B and B′). In contrast, neither a nonlocalized mRNA, *gapdh*, nor a germ granule mRNA, *nos1*, are enriched in the vegetal RNA bodies (Figure 1, C–F); *gapdh* is uniformly distributed throughout the oocyte cytoplasm (Figure 1C′), while *nos1*, having been localized earlier in oogenesis, is tightly deposited at the vegetal cortex (Figure 1, E′ and E″). Interestingly, while not enriched, *gapdh* RNA is not excluded from the vegetal RNA clusters (Figure 1, D and D′). Our results show that during localization, vegetally transported mRNAs are restricted to nonexclusive, heterotypic bodies, hereafter termed L-bodies.

To determine whether well-characterized *vg1* RBPs are components of L-bodies, we performed combined FISH and immunofluorescence (FISH-IF) for Stau1 (Staufen 1; Yoon and Mowry, 2004), hnRNPAB (40LoVE; Czaplinski *et al.*, 2005), and Vera (Igf2bp3; Deshler *et al.*, 1998; Havin *et al.*, 1998). Stau1 (Figure 1, G–I) and Vera (Figure S2A-B) are enriched in, but not restricted to, L-bodies. By comparison, hnRNPAB shows dramatic enrichment in L-bodies in the vegetal cortical cytoplasm (Figure 1, J–L). These results indicate that L-bodies are large RNPs that contain vegetally localizing RNAs.

Localized RNAs are specifically enriched in L-bodies

Localization of *vg1* mRNA can be recapitulated by a localization element (*LE*) that is composed of a duplication of the first 135 nucleotides of a larger element residing in the *vg1* mRNA 3′ UTR (Gautreau *et al.*, 1997; Lewis *et al.*, 2008). Microinjected *LE* RNA is enriched in the vegetal cytoplasm (Figure 2A) and is both copackaged with endogenous *vg1* mRNA in the vegetal cytoplasm (Figure 2A′) and incorporated into L-bodies (Figure 2, B and B′). By contrast, a mutant version of the *LE* RNA (*mutLE*) harboring point mutations that ablate specific RBP binding (PTB and Vera; Lewis *et al.*, 2008) is not capable of vegetal localization (Figure 2C) and fails to accumulate in L-bodies (Figure 2 D and D′). These results indicate that enrichment into L-bodies is mediated by sequence-specific features of target RNAs and that such enrichment is required for subsequent vegetal RNA localization.

Composition of L-bodies

To further analyze the RNA and protein components of L-bodies we took a biochemical approach. First, we cross-linked stage II–III oocytes with formaldehyde to reduce loss of L-body components during fractionation and to minimize nonphysiological interactions after lysis (Mili and Steitz, 2004). We then fractionated lysates prepared

vegetal cortex at the bottom. Combined FISH-IF was used to detect *vg1* mRNA (magenta) and hnRNPAB protein (J′, green). Scale bar = 50 µm. (K) Combined FISH-IF was used to detect hnRNPAB (K, green) in the vegetal cytoplasm of a stage II oocyte, merged with *vg1* mRNA (magenta) in K′. Scale bar = 20 µm. (L) High magnification view of the vegetal cytoplasm of a stage II oocyte showing colocalization of *vg1* mRNA (magenta) and hnRNPAB protein (green). Scale bar = 10 µm.

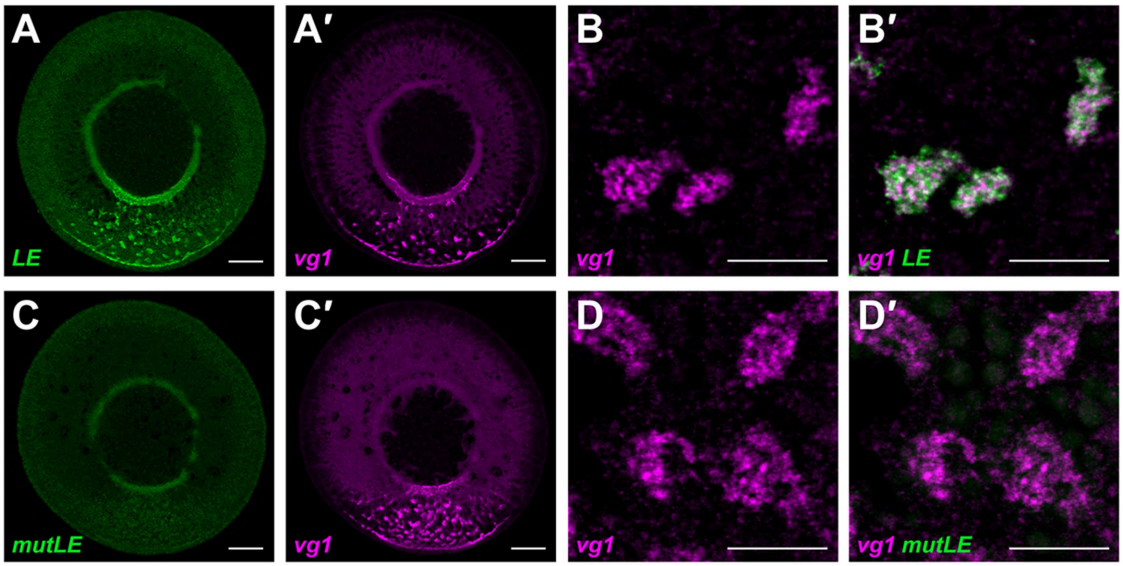

FIGURE 2: Assembly into L-bodies is correlated with vegetal localization. (A) A cryosection of a stage II oocyte is shown, with microinjected fluorescently labeled *LE* RNA (green) and endogenous *vg1* mRNA (A′) detected by FISH (magenta). The vegetal cortex at the bottom, and the scale bar = 50 µm. (B) High magnification view of the vegetal cytoplasm of a stage II oocyte with endogenous *vg1* mRNA (magenta) detected by FISH and microinjected *LE* RNA (green) shown merged in B′. Scale bar = 10 µm. (C) A cryosection of a stage II oocyte is shown, with microinjected fluorescently labeled mutant *LE* RNA (*mutLE*) in green and endogenous *vg1* mRNA (C′) detected by FISH in magenta. The vegetal cortex at the bottom and the scale bar = 50 µm. (D) High magnification view of the vegetal cytoplasm of a stage II oocyte with endogenous *vg1* mRNA (magenta) detected by FISH and microinjected *mutLE* RNA (green) shown merged in D′. Scale bar = 10 µm.

from the cross-linked stage II–III oocytes using SE chromatography (Figure 3A). Using this approach, both endogenous *vg1* mRNA and microinjected *LE* RNA chromatograph as large complexes in the void volume, while microinjected nonlocalized RNAs, *mutLE* and *β-globin*, do not (Figure 3B). Known *vg1* RBPs, Vera, Stau1, and hnRNPAB, also chromatograph as large complexes (Figure 3, C and D). Treatment of the oocyte lysate with RNase prior to SE chromatography causes *vg1* RBPs, including Vera (Figure 3C), to chromatograph in fractions containing smaller complexes, indicating that the large complexes are RNPs. By contrast, Tubulin chromatographs in fractions containing small complexes regardless of RNase treatment (Figure 3C). Coimmunoprecipitation (co-IP) analyses using fractions pooled from the void volume after SE chromatography (Figure 3D) demonstrate that Vera, Stau1, and hnRNPAB all co-IP *vg1* mRNA (Figure 3E) and with one another (Figure 3F). These results, along with the colocalization analyses shown in Figure 1, G–L, and Supplemental Figure S2, indicate that *vg1* mRNA, Vera, hnRNPAB, and Stau1 are packaged together in L-bodies.

To purify L-bodies, the pool (Figure 3D) of SE fractions containing large complexes was subjected to parallel IP using two known *vg1* RBPs, Stau1 and hnRNPAB (Figure 3A), which are both enriched in L-bodies as assessed by FISH-IF (Figure 1, G–L) and SE chromatography (Figure 3D). Stau1 and hnRNPAB, like other characterized *vg1* RBPs, are known to have multiple roles in RNA biogenesis and are not solely involved in vegetal mRNA localization (Yisraeli, 2005; Snedden *et al.*, 2013; Heraud-Farlow and Kiebler, 2014). Therefore, we reasoned that requiring interactions with two different *vg1* RBPs would more accurately identify constituents specific to L-bodies. In addition, hnRNPAB is not enriched in the Balbiani body (Boke *et al.*, 2016), allowing us to biochemically distinguish L-bodies from *Xenopus* germ granules. Both RNA-seq and liquid chromatography-tandem mass spectrometry (LC-MS/MS) were performed on Stau1 and hnRNPAB IPs, with IgG as the negative control.

For RNA-seq analysis, candidate L-body RNAs were required to be at least 1.8-fold enriched over IgG in both the Stau1 and the hnRNPAB RNA-IPs, with a q value < 0.05 (Figure 3G; Supplemental Table S1); several were validated by RT-qPCR (Supplemental Table S2). The list of L–body-enriched RNAs generated by our analysis (Supplemental Table S1) contains 21 mRNAs, including *vg1* mRNA, that have been demonstrated to be vegetally localized in other studies, but none of the ~20 mRNAs that are known to be localized earlier in oogenesis through a Balbiani body-dependent pathway, such as *nos1*. The newly identified vegetal RNAs include 17 predicted noncoding RNAs, which represent three of the top four most highly enriched L-body RNAs (Supplemental Tables S1 and S2). MEME motif analysis of L-body-enriched RNAs revealed enrichment of pyrimidine-rich sites, which may correspond to PTB-binding sites (Supplemental Table S3). This is notable, as *LE* RNAs carrying mutations that abolish PTB and/or Vera binding fail to incorporate into L-bodies (Figures 2 and 3B; Lewis *et al.*, 2008). Vera binding motifs were not uncovered by the MEME analysis, possibly due to the degeneracy of the Vera binding site (Supplemental Table S2; Deshler *et al.*, 1998). Gene ontology (GO) analysis revealed categories that are consistent with regulatory roles in early development (Supplemental Table S4).

L-bodies contain proteins found in other classes of cytoplasmic RNP granules

Our LC-MS/MS analysis results identified a set of 86 proteins that represent potential L-body components (Figure 3H). Enrichment of at least twofold over the IgG control in both the Stau1 and the hnRNPAB IPs was the required threshold for candidate proteins. The L-body proteome (Figure 4A) contains all known *vg1* RBPs: Elavl1, Elavl2, hnRNPAB (40LoVE), Vera (Igf2bp3), PTB (Ptbp1), Stau1, and Stau2 (Deshler *et al.*, 1998; Havin *et al.*, 1998; Cote *et al.*, 1999; Allison *et al.*, 2004; Yoon and Mowry, 2004;

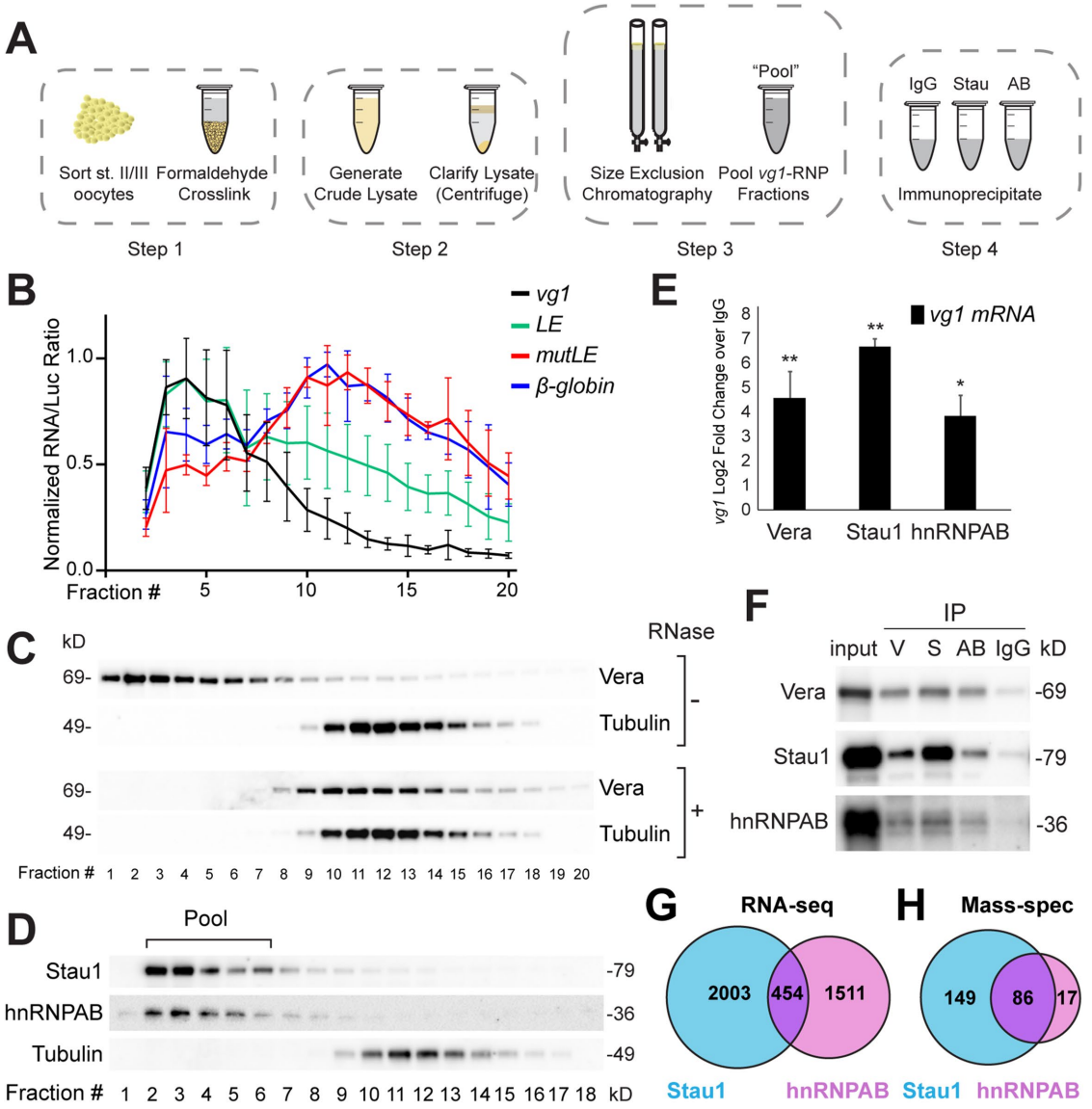

FIGURE 3: Isolation of L-bodies. (A) Schematic of the L-body isolation procedure. Stage II/III oocytes were formaldehyde cross-linked, homogenized, clarified by centrifugation, and fractionated by SE chromatography. Fractions containing *vg1* mRNA were pooled and divided equally for immunoprecipitations using anti-Stau1 (Stau) and anti-hnRNPAB (AB) antibodies, with IgG as a negative control. (B) Stage II–III oocytes were microinjected with *LE* RNA (green), nonlocalizing *mutLE* RNA (red), and nonlocalizing *β-globin* RNA (blue). Oocyte lysates were subjected to SE chromatography and the levels of the microinjected RNAs and endogenous *vg1* mRNA (black) were measured in SE column fractions by RT-qPCR, normalized to *luciferase* control RNA (*luc*). Error bars represent standard error of the mean (SEM); $n = 4$ columns. (C) Oocyte lysate was treated with RNase A prior to SE chromatography, followed by immunoblot analysis with anti-Vera and anti-Tubulin antibodies. Column fractions from untreated (–) lysate are shown at the top and column fractions from RNase-treated (+) lysate are shown at the bottom. (D) Immunoblot analysis is shown, of SE column fractions probed with anti-Stau1, anti-hnRNPAB, and anti-Tubulin. The input (load) is at the left and fraction numbers are shown at the bottom. Stau1 and hnRNPAB chromatograph primarily in the void volume; fractions 2–5, which were pooled for further purification. (E) Pooled SE column fractions (2–5) were immunoprecipitated (IPed) using anti-Vera, anti-Stau1, anti-hnRNPAB, and IgG. Following isolation of bound RNA, *vg1* RNA was detected by RT-qPCR, with normalization to a *luciferase* RNA control. Shown is log2-fold enrichment for *vg1* RNA from the Vera, Stau1, and hnRNPAB co-IPs over IgG. $n = 5$ and error bars represent SEM. $^{**}p < 0.01$, $^{*}p < 0.05$. (F) Pooled SE column fractions (2–5) were IPed using anti-Vera (V), anti-Stau1 (S), anti-hnRNPAB (AB), and IgG. After SDS–PAGE, co-IP of Vera, Stau1, and hnRNPAB were confirmed by immunoblotting with anti-Vera, anti-Stau1, and anti-hnRNPAB. (G) RNA-seq was performed on parallel IPs using anti-Stau1, anti-hnRNPAB, and IgG. A Venn diagram shows the overlap between hnRNPAB (magenta) and Stau1 (blue); 454 RNAs were identified as enriched over IgG in both the hnRNPAB and Stau1 IPs. See also Tables S1-S4. (H) MS was performed on parallel IPs using anti-Stau1, anti-hnRNPAB, and IgG. A Venn diagram shows the overlap between hnRNPAB (magenta) and Stau1 (blue); 86 proteins were identified as significantly enriched over IgG in both the hnRNPAB and Stau1 IPs.

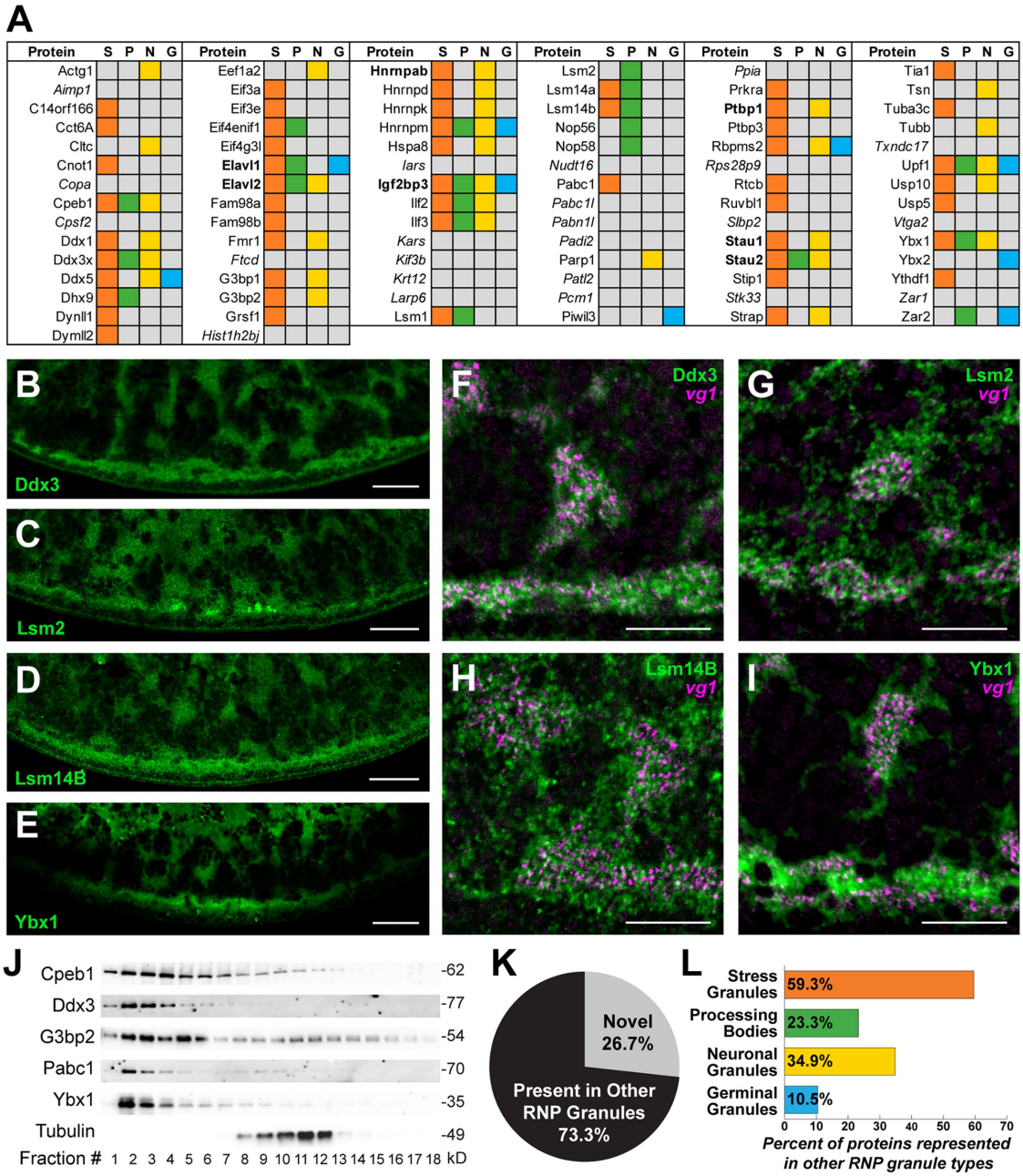

FIGURE 4: L-bodies contain protein components common to other classes of cytoplasmic RNP granules. (A) Protein constituents of L-bodies are also found in stress granules (S, orange), P-bodies (P, green), neuronal granules (N, yellow), and germ granules (G, blue). Proteins found in L-bodies but not reported in other granules, are italicized and previously known *vg1* RBPs are bolded. (B–I) IF and combined FISH-IF were performed to validate potential protein constituents of L-bodies. (B, C) Shown are IF images of stage II oocytes using (B) anti-Ddx3, (C) anti-Lsm2, (D) anti-Lsm14B, and (E) anti-Ybx1. The vegetal cortex is at the bottom; scale bars = 20 µm. (F–I) Shown are FISH-IF images of the vegetal cytoplasm of stage II oocytes with the vegetal cortex at the bottom; scale bars = 10 µm. Shown in magenta is *vg1* mRNA detected by FISH. Merged in green is IF using (F) anti-Ddx3, (G) anti-Lsm2, (H) anti-Lsm14B, and (I) anti-Ybx1. See also Supplemental Table S5. (J) Immunoblot analysis is shown of SE column fractions probed using anti-Cpeb1, anti-Ddx3, anti-G3bp2, anti-Pabc1, anti-Ybx1, and anti-Tubulin antibodies. The fraction numbers are indicated at the bottom. (K) Overlap (black, 73.3%) of L-body constituents with other cytoplasmic granules; unique proteins are indicated by gray (26.7%). (L) The percentage of identified L-body proteins that are found in other cytoplasmic RNP granule types: stress granules (59.3%, 51 of 86), P-bodies (23.3%, 20 of 86), neuronal granules (34.9%, 30 of 86), and germinal granules (10.5%, 9 of 86). See also Supplemental Table S7.

Colegrove-Otero *et al.*, 2005; Czaplinski *et al.*, 2005; Arthur *et al.*, 2009). The presence of both Dynein (Dynll1 and Dynll2) and Kinesin (Kif3b) subunits is also notable, as both Dynein and Kinesin II have been shown to be required for vegetal RNA transport (Betley *et al.*, 2004; Messitt *et al.*, 2008; Gagnon *et al.*, 2013). Notably absent is Xvelo, which is the definitive Balbiani body marker protein (Boke *et al.*, 2016). The success in isolating the known *vg1*-interacting proteins and stringent thresholds for analyses gives a

high degree of confidence that the remaining 76 proteins represent newly identified L-body components.

Putative L-body components were validated by FISH-IF, IF, and SE chromatography (Figure 4, B–J, and Supplemental Table S5). L-body proteins are found in large *vg1* mRNA-containing structures, as shown by FISH-IF for four examples in Figure 4: Ddx3 (Figure 4, B and F), Lsm2 (Figure 4, C and G), Lsm14B (Figure 4, D and H), and Ybx1 (Figure 4, E and I). FISH-IF validation was also performed for an additional 26 putative L-body proteins, as summarized in Supplemental Table S5. Analysis by SE chromatography shows that L-body proteins elute in the void volume (Figure 4J) in large complexes that are sensitive to RNase treatment (Supplemental Table S5). Using these approaches, we validated 35 of the putative L-body components listed in Figure 4A (Supplemental Table S5). GO analysis (Supplemental Table S6) revealed that four of the five top GO-categories are related to nucleic acid binding, with the top category being RNA binding. ATP binding is significantly enriched as well, contributed in part by the four DEAD-box helicases identified in L-bodies (Figure 4A), which may act in RNP remodeling through their ability to unwind RNA and alter RNA–protein interactions (Gilman *et al.*, 2017).

A striking feature of the L-body proteome is the abundance of proteins that are known components of previously described cytoplasmic RNP granules, including stress granules, P-bodies, neuronal granules, and germ granules (designated S, P, N, and G, respectively; Figure 4, A, K, and L; Supplemental Table S7). Remarkably, the majority (73.3%) of the identified L-body components are present in at least one other RNP granule type (Figure 4K), with 31 of those (36%) being found in more than one RNP granule type (Figure 4, A and L). The remaining proteins (26.7%) appear to be novel to L-bodies (Figure 4K) and could provide functional specificity. Taken together, these results indicate that L-bodies represent a new class of cytoplasmic RNP granule.

Dynamics of L-body RNAs and proteins differ in vivo

Because many proteins found in cytoplasmic RNP granules contain IDRs (Mittag and Parker, 2018; Uversky, 2017), we examined the prevalence of IDRs in the L-body proteome. Using SLIDER (Peng *et al.*, 2014), a predictive tool for IDRs, we found the majority (74%) of all L-body components contain a putative IDR, which is a significant enrichment over the *Xenopus* proteome (56%; Figure 5A). Other types of cytoplasmic RNP granules have been described as phase-separated bodies, with constituent proteins and mRNAs exhibiting liquidlike behavior in some RNP granules and gel- or amyloidlike properties in others (reviewed in Alberti and Hyman, 2016; Shin and Brangwynne, 2017; Boeynaems *et al.*, 2018). Intriguingly, prionlike domains, which are a specialized category of IDRs that are overrepresented in gel- and amyloidlike structures, are also overrepresented in the L-body proteome (Figure 5B). To probe the properties of L-bodies, we first stained oocyte sections with thioflavin, a dye that exhibits a selective fluorescence shift in the presence of cross-beta strands, which are characteristic of amyloid structures (Guntern *et al.*, 1992). The vegetal oocyte cytoplasm stains richly with thioflavin (Figure 5C), revealing a meshlike substructure evident at high magnification (Figure 5D). To test whether the thioflavin-staining structures correspond to L-bodies, we next used combined FISH and thioflavin staining to ask whether vegetally localized RNAs colocalize with the meshlike structures. Localized mRNAs, *vg1* (Figure 5E) and *vegT* (Figure 5F), are highly coincident with the thioflavin staining. By contrast, nonlocalized *gapdh* mRNA is not colocalized with the thioflavin staining (Figure 5G). Because thioflavin may also stain dense networks of RNA structure (Xu *et al.*, 2016), we next tested whether *Xenopus* oocyte RNA is capable of staining with thioflavin. Indeed, *Xenopus* oocyte RNA, which forms droplets at low concentrations and gels at high concentrations (Supplemental Figure S3, A and B), binds to thioflavin in a time- and concentration-dependent manner (Supplemental Figure S3C). Although thioflavin staining can be challenging to interpret, these results suggest that L-bodies may contain amyloidlike components.

To examine the dynamics of L-bodies in vivo, protein mobility was assessed by fluorescence recovery after photobleaching (FRAP) in live oocytes. In these experiments, we marked L-bodies by microinjection of fluorescently labeled *LE* RNA into stage II oocytes along with mRNA expressing mCherry (mCh)-tagged L-body proteins (Figure 6, A and B). To determine dynamics within the L-bodies, partial granule FRAP was performed on three previously known L-body proteins (hnRNPAB, Stau1, and Vera) as well as a newly identified constituent, Ybx1 (Tafuri and Wolffe, 1990). Each of these proteins contains at least one RNA-binding domain, and both hnRNPAB and Ybx1 also contain IDRs. Each of the four RBPs exhibited significant mobility within the L-body, with hnRNPAB showing the highest mobile fraction (94.2%) and Vera having the lowest (52.9%; Figure 6A). These data indicate that protein constituents of L-bodies are dynamic.

To examine the dynamics of L-body RNAs in vivo, we performed FRAP on microinjected RNAs. Both *vg1 LE* (*LE*) and *vegT LE* (*TLE*) RNAs are highly immobile in vivo, with mobile fractions of 4% and 19%, respectively (Figure 6, C–E). In contrast, nonlocalized RNAs are much more dynamic; the mobile fractions for *mutLE* RNA and *gapdh* mRNA are 61.2 and 56.1%, respectively (Figure 6E). Notably, mobility does not correlate with length of either the proteins or the RNAs (Supplemental Table S8). The low mobility of localized RNAs compared with the dynamic behavior of constituent proteins (Figure 6F) suggests at least two distinct phases within L-bodies, with a potentially solid- or gellike RNA-containing phase enveloped in a dynamic protein-containing phase.

DISCUSSION

In this work, we have discovered that vegetal mRNA localization in *Xenopus* oocytes proceeds via the formation of L-bodies, which are a new class of cytoplasmic RNP granule. We base this conclusion on several lines of evidence: First, L-bodies are large cytoplasmic RNPs that are specifically enriched for vegetally localized mRNAs. Second, incorporation of these localized mRNAs into L-bodies is determined by *cis*-elements within mRNAs and enrichment is required for subsequent localization. Third, the protein composition of purified L-bodies exhibits a high degree of similarity to that of other classes of cytoplasmic RNP granules. In addition to over two-thirds of the proteins being directly conserved amongst cytoplasmic RNP granules, the overrepresentation of multivalent RBPs and IDR-containing proteins provides a compositional link between L-bodies and other classes of phase-separated RNPs (reviewed in Banani *et al.*, 2017; Shin and Brangwynne, 2017; Gomes and Shorter, 2019; Dodson and Kennedy, 2020). Finally, we find that L-body components display varying dynamics, with comparatively dynamic proteins and nondynamic localized RNAs.

Maternal mRNAs are localized within developing oocytes of *Xenopus* and many other species where their local translation is critical for proper embryonic patterning. Our work suggests that such cargos in *Xenopus* oocytes are large cytoplasmic RNP granules. We find that L-bodies contain many copies of localized mRNAs (Figure 1), which contrasts with some other types of transport cargos where mRNAs are packaged singly (Batish *et al.*, 2012; Buxbaum *et al.*, 2014; Little *et al.*, 2015) or in homotypic clusters (Niepielko *et al.*, 2018; Trcek *et al.*, 2020). Importantly, vegetally localized RNA

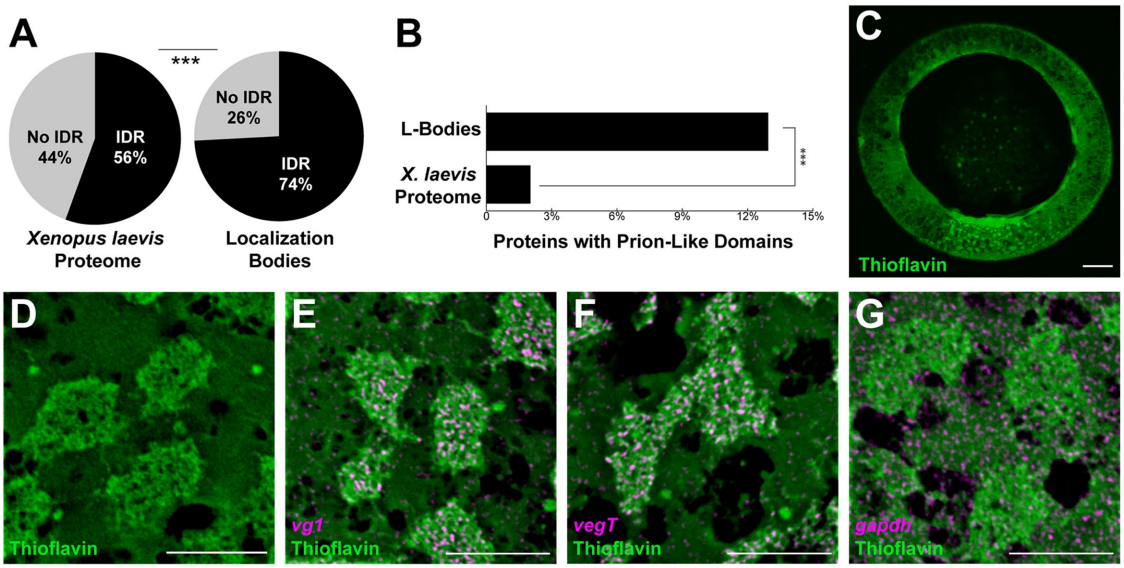

FIGURE 5: L-bodies exhibit a meshlike structure. (A) Comparison by SLIDER analysis (Peng *et al.*, 2014) for long IDRs (>30 consecutively disordered residues) for the *X. laevis* proteome vs. the L-body proteome. ***$p < 0.001$. (B) The percentage of prionlike domains in the L-body proteome was compared with the *Xenopus* proteome using PLAAC. Prionlike domains are sixfold enriched in L-bodies (12.9%) relative to the *Xenopus* proteome (2.02%). ***$p < 0.001$. (C) A stage II oocyte stained with thioflavin is shown, with the vegetal cortex at the bottom. Scale bar = 50 µm. (D) High magnification view of the vegetal cytoplasm of a stage II oocyte stained with thioflavin. Scale bar = 10 µm. (E–G) High magnification views of the vegetal cytoplasm of stage II oocytes stained with thioflavin are shown; scale bars = 10 µm. Thioflavin staining (green) was combined with FISH (magenta) for detection of the following RNAs: (E) *vg1*, (F) *vegT*, and (G) *gapdh*.

sequences are specifically enriched in L-bodies, while nonlocalizing RNAs are not (Figures 1–2), suggesting that packaging into L-bodies is required for vegetal mRNA localization. New insight into the molecular and physical nature of these structures came from our purification and MS results, which revealed that L-bodies contain protein constituents that are shared among many cytoplasmic RNP granules (Figures 3–4; Supplemental Table S7). Taken together, these results show that vegetal mRNAs are organized in L-bodies, which are a new type of cytoplasmic RNP.

While L-bodies contain protein constituents that are found in other types of cytoplasmic RNP granules (Figure 4A), our results argue that L-bodies are distinct from stress granules, P-bodies, germ granules, and other cytoplasmic RNP granules such as RNase L-bodies (Burke *et al.*, 2020), as more than a quarter (26.7%) of the identified L-body proteins are not found in these other RNP granule types. Proteins unique to L-bodies include a cytokeratin protein (Krt12), which could be involved in anchoring to the vegetal cortex, as cytokeratin proteins have been implicated in this process (Kloc *et al.*, 2005); a Kinesin II subunit (Kif3a), which has been shown to play a role in vegetal RNA transport in *Xenopus* oocytes (Betley *et al.*, 2004; Messitt *et al.*, 2008); and a peptidyl arginine deiminase (Padi2), for which there is an oocyte-specific paralog (Padi6) in mice (Liu *et al.*, 2017). Our results also indicate that L-bodies are distinct from *Xenopus* germ granules, or Balbiani bodies. The Balbiani body is a prominent structure found exclusively in stage I oocytes, which is deposited at the vegetal cortex during stage I of *Xenopus* oogenesis, before L-bodies are evident during stages II–III (Oh and Houston, 2017). The Balbiani body contains mRNAs such as *nos1*, which are important for germline specification (Oh and Houston, 2017), as well as Xvelo protein, which is the definitive marker of the Balbiani body and has been implicated in assembly of this amyloidlike structure (Boke *et al.*, 2016). Xvelo protein, along with *nos1* and other mRNAs localized in stage I through the Balbiani body pathway, are notably absent from the L-body proteome (Figure 4A) and the L-body transcriptome (Supplemental Table S1), indicating that L-bodies are distinct from Balbiani bodies. Localizing RNAs are a defining feature of L-bodies (Figure 1, A and B; Supplemental Figure S1). Our FISH-IF validation of L-body proteins (30 proteins) indicates that each of these proteins is colocalized with *vg1* RNA in L-bodies (Supplemental Table S5), but it remains to be determined whether all putative L-body proteins are present in all L-bodies. It is possible that some L-body proteins are associated only with a subset of L-bodies, possibly due to specific roles in maturation and/or assembly of L-bodies during different steps of the RNA localization pathway.

A substructure of L-bodies is apparent on staining with thioflavin (Figure 5), a dye that typically stains amyloidlike aggregates formed by protein β-sheet interactions (Guntern *et al.*, 1992; Nilsson, 2004). While our efforts to identify protein components with both structured patterns of L-body localization and nondynamic intragranule motility did not provide insights into the basis for the meshlike substructure, it is possible that the substructure could, at least in part, be composed of RNA. This is particularly intriguing given recently observed functions for mRNA structure in liquid–liquid phase separation and transitions to gel- or solidlike phases (Jain and Vale, 2017; Langdon *et al.*, 2018; Van Treeck *et al.*, 2018). RNA–RNA interactions have also been implicated in RNA transport and localization. In *Drosophila* oocytes, homotypic intermolecular RNA–RNA interactions are necessary for localization of *bicoid* and *oskar* mRNAs (Ferrandon *et al.*, 1997; Jambor *et al.*, 2011). In *Xenopus* oocytes, depletion of *vegT* mRNA, an L-body component, leads to the mislocalization of *vg1* mRNA (Heasman *et al.*, 2001), suggesting a role for heterotypic mRNA interactions. Thioflavin has been demonstrated to recognize dense networks of RNA structure (Xu *et al.*, 2016), offering the possibility that RNA may be one source of thioflavin staining observed in L-bodies. It is also possible that protein amyloid structures, such as shown for Xvelo protein in *Xenopus*

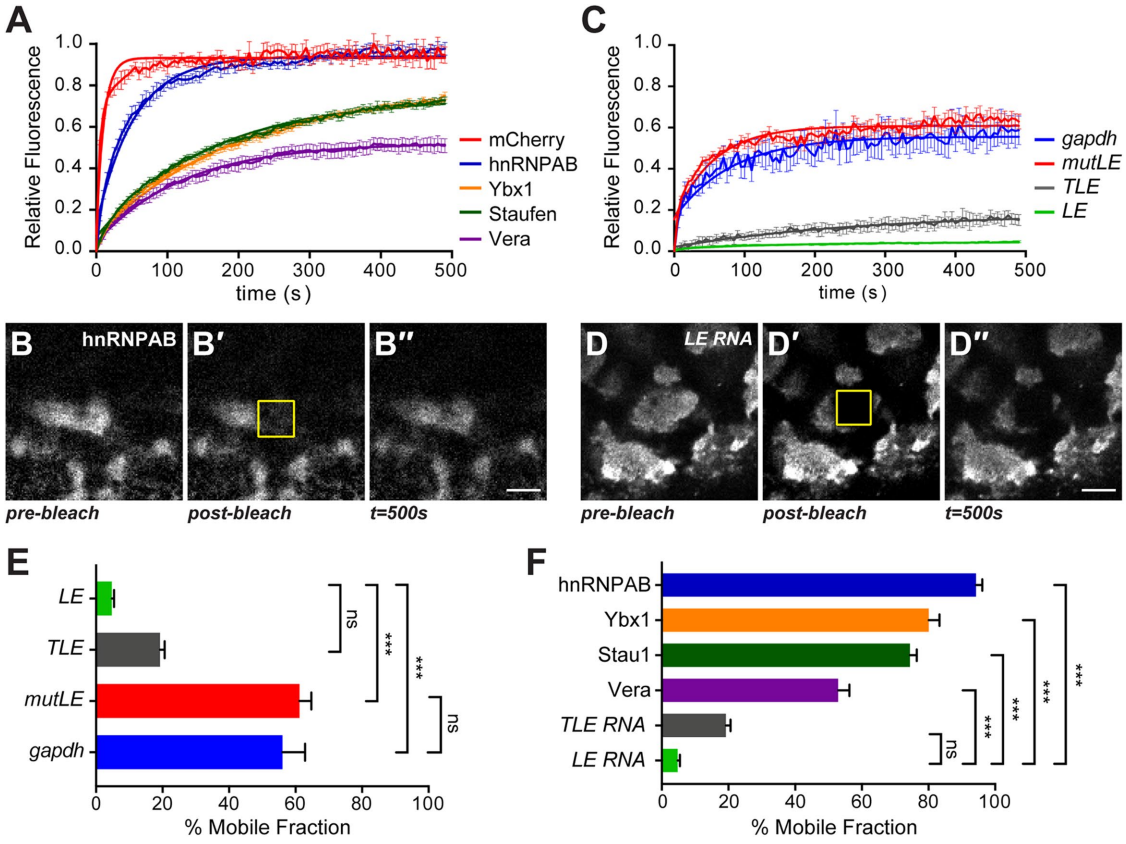

FIGURE 6: L-bodies contain dynamic proteins and nondynamic localized RNAs. (A) Stage II oocytes expressing mCh, or the following mCh-tagged proteins: hnRNPAB, Ybx1, Stau1, and Vera, were microinjected with Cy5-labeled *vg1 LE* RNA to mark L-bodies. Recovery curves are shown for mCh (red), mCh-hnRNPAB (blue), Ybx1-mCh (orange), Stau1-mCh (green), and Vera-mCh (purple). Error bars indicate standard error of the mean (SEM). (B) An image of the vegetal cytoplasm of an oocyte microinjected with mCh-hnRNPAB is shown, with a 10 μm^2 ROI (yellow); scale bar = 10 μm. B′ and B″ show the postbleach and 500 s time points, respectively. Photobleaching was corrected using the ImageJ plugin CorrectBleach V2.0.2. Zenodo (Miura *et al.*, 2014) (C) Stage II oocytes were microinjected with Cy3-labeled *vg1 LE* RNA to mark L-bodies and coinjected with the following Cy5-labeled RNAs for FRAP analysis: *gapdh*, mutated *vg1 LE* (*mutLE*), *vegT LE* (*TLE*), or *vg1 LE* (*LE*). Recovery curves are shown for *gapdh* RNA (blue), *mutLE* RNA (red), *TLE* RNA (gray), and *LE* RNA (green). Labeling of RNAs with Cy3 vs. Cy5 does not affect dynamics (see Figure S4). Error bars show SEM. (D) An image of the vegetal cytoplasm of an oocyte microinjected with Cy5-labeled *LE* RNA is shown, with a 10 μm^2 ROI (yellow); scale bar = 10 μm. D′ and D″ show the postbleach and 500 s time points, respectively. Photobleaching was corrected using the ImageJ plugin CorrectBleach V2.0.2. Zenodo (Miura *et al.*, 2014) (E) The mobile fraction is shown for *LE* RNA (green, 4.8 ± 0.6%), *TLE* RNA (gray, 19.2 ± 1.4%), *mutLE* RNA (red, 61.2 ± 3.6%), and *gapdh* RNA (blue, 56.1 ± 6.7%), determined by FRAP as in panel C. The results from 7 oocytes per RNA are shown and error bars show SEM. P-values were calculated using one-way ANOVA with Tukey's multiple comparison correction; ***$p < 0.001$, ns is not significant. (F) The mobile fraction for mCh-hnRNPAB (blue, 94.2 ± 1.9%), Ybx1-mCh (orange, 80.1 ± 3.2%), Stau1-mCh (dark green, 74.5 ± 2.0%), Vera-mCh (purple, 52.9 ± 3.4%), *TLE* RNA (gray, 19.2 ± 1.4%), and *LE* RNA (green, 4.8 ± 0.6%) was determined by FRAP, as in panels A and C. The results from seven oocytes per protein and RNA are shown and error bars indicate SEM. *P* values were calculated using one-way ANOVA with Tukey's multiple comparison correction; ***$p < 0.001$, ns is not significant.

Balbiani bodies (Boke *et al.*, 2016), may be the source of thioflavin staining. Although Xvelo is not present in L-bodies, other amyloid-forming proteins may await identification.

Our in vivo imaging results reveal L-bodies to be biomolecular condensates that contain both nondynamic RNAs and dynamic proteins. The coexistence of both a liquidlike dynamic phase and a gel- or solidlike phase have been observed in other biomolecular condensates such as P granules (Putnam *et al.*, 2019) and stress granules (Jain *et al.*, 2016) and may reflect a fundamental aspect of RNP granule organization. However, unlike in these examples, our findings show that RNA is a nondynamic phase in L-bodies, as it is the localized RNAs that are nondynamic (Figure 6). While RNA has been viewed as a multivalent platform, capable of mediating intermolecular interactions between *trans*-acting proteins, recent studies have challenged this ancillary role for RNA in granule organization and offered new roles for RNA–RNA interactions in defining the composition of RNP granules (Jain and Vale, 2017; Van Treeck *et al.*, 2018; Langdon *et al.*, 2018; Niepielko *et al.*, 2018; Trcek *et al.*, 2020). In L-bodies, the specific enrichment and low dynamics of localized RNAs raise the possibility that RNA may play a critical role in the organization of this biomolecular condensate.

The extremely low mobility of localized RNAs within L-bodies further suggests an important distinction between the localizing RNA-containing portion of this RNP granule and nonlocalizing

RNAs. While nonlocalized mRNAs are not concentrated within the L-body, they are not excluded (Figures 1-2). Interestingly, nonlocalizing mRNAs, including the length-matched mutant *vg1 LE* (*mut-LE*) and *gapdh*, may also remain in dynamic exchange with the surrounding cytoplasm (Figure 6). Incorporation into L-bodies relies on sequence-encoded features of the RNAs (Figure 2), which interact with the sequence-specific *vg1* RBPs, PTB and Vera (Lewis *et al.*, 2008). Thus, both RNA sequences and specific RBPs are important for RNA enrichment in L-bodies. Importantly, the observation that sequence mutations within the *vg1 LE* that are known to ablate localization (Lewis *et al.*, 2008) also block L-body enrichment (Figure 2) functionally links L-bodies to mRNA localization.

We propose a model for L-body strsucture and assembly (Figure 7). Interactions between specific RBPs and sequence motifs in localized RNAs both promote the local enrichment of L-body factors and control specific incorporation of localized mRNAs into L-bodies. As localized RNAs become strongly enriched, high RNA concentrations promote RNA–RNA interactions and the formation of a solid- or gel-like RNA phase. The nondynamic RNA phase may act as a multivalent scaffold or, alternatively, an unidentified protein or proteins may serve instead as a scaffold in L-bodies. In this model, protein constituents are enriched in L-bodies through their interaction with the nondynamic scaffold; some are highly dynamic due to their weak interactions with the scaffold, while RBPs that interact more strongly with the nondynamic RNA phase display intermediate dynamics. By contrast, nonlocalized RNAs and other proteins, which lack the capacity to interact with the nondynamic scaffold, freely diffuse in and out of L-bodies.

By defining RNA–protein condensates (L-bodies) as a driver of vegetal RNA localization in *Xenopus* oocytes, regulation of distinct transport and developmental steps can be understood in the context of the unique physical properties of phase-separated structures. Cytoplasmic RNP granule components have been observed to transition between diffuse, liquidlike, or more solid states in response to environmental cues that regulate coassembly, viscosity, and demixing specificity within granules (Hubstenberger *et al.*, 2013; Wang *et al.*, 2014; Jain *et al.*, 2016; Han *et al.*, 2018; Putnam *et al.*, 2019). In this way, the innately reversible interactions that underlie RNP granule composition allow for fine-tuning of RNP granule dynamics, which can be exploited as a regulatory mechanism. In oocytes, which are noncycling for protracted periods of time, packaging of maternal mRNAs into nondynamic gel- or solidlike RNP granules, such as L-bodies, may be an important mechanism to silence translation over long time frames. On response to appropriate developmental cues, these stable RNP granules must then be disassembled. The mechanisms regulating stabilization and disassembly in oocytes are likely to represent a general paradigm for understanding regulation of dynamic phase transitions in space and time.

MATERIALS AND METHODS

Request a protocol through *Bio-protocol*.

Oocyte isolation and culture

Oocytes were harvested from *X. laevis* females, either J Strain (NXR, catalogue # NXR_0024) or wild type (Nasco, catalogue # LM00535MX). All animal experiments were approved by the Brown University Institutional Animal Care and Use Committee. Oocytes were enzymatically defolliculated in 3 mg/ml collagenase (Sigma) followed by washes in MBSH (88 mM NaCl, 1 mM KCl, 2.4 mM $NaHCO_3$, 0.82 mM $MgSO_4$, 0.33 mM $CaCl_2$, 0.33 mM $Ca(NO_3)_2$, 10 mM HEPES, pH7.6). Stage II–III oocytes were cultured at 18°C in XOCM (50% Leibovitz L-15 [Thermofisher], 15 mM HEPES [pH 7.6], 1 mg/ml insulin, 50 U/ml nystatin, 100 U/ml penicillin/streptomycin, 0.1 mg/ml gentamicin).

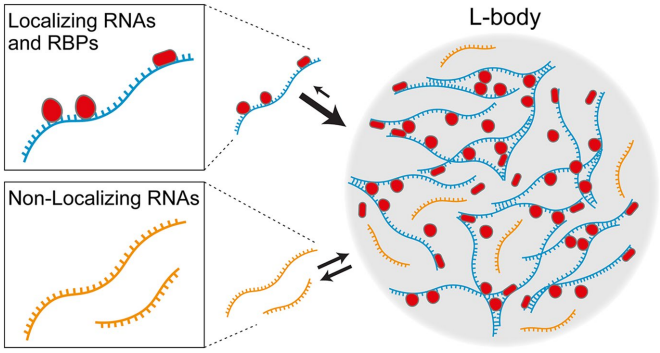

FIGURE 7: Model for L-body structure and assembly. Localizing RNAs (blue) interact with specific RNA-binding proteins (RBPs; red) that facilitate local enrichment. Nonlocalizing RNAs (gold) lack binding sites for these RBPs and do not condense with other localized RNAs. Specific RBPs facilitate enrichment (large arrows) of localized RNAs in L-bodies (gray). L-body enrichment results in high local RNA concentrations, facilitating RNA–RNA, RNA–protein, and protein–protein interactions and formation of a nondynamic RNA phase enmeshed in a more dynamic protein phase. Nonlocalized RNAs (and proteins) are not excluded from L-bodies, and can freely move in and out (double arrows).

RNA transcription and microinjection

Fluorescently labeled RNAs, *vg1 LE* (Gautreau *et al.*, 1997), *vegT LE* (*TLE*) (Bubunenko *et al.*, 2002), nonlocalizing mutant *vg1 LE* (*mutLE*) (Lewis *et al.*, 2008), and *βglobin* (Krieg and Melton, 1984) were generated from linearized plasmids pSP73-2 × 135, pSP73-VegTLE, pSP73-VLEΔE2ΔVM1, and pSP64-XβM, respectively. For transcription of *gapdh*, a PCR product was generated using gapdh-specific primers (gapdh T7 Fwd and gapdh Rev), with the forward primer containing the T7 promoter sequence (Supplemental Table S9). Barcoded RNAs were generated from PCR products using pSP73-2 × 135, pSP73-VLEΔE2ΔVM1, and pSP64-XβM plasmids as templates and the following "barcode" primers: LE barcode A Fwd, mutLE barcode B Fwd, LE/mutLE Rev, βglobin barcode A Fwd, βglobin barcode B Fwd, βglobin barcode C Fwd, and βglobin Rev (Supplemental Table S9). Transcription was performed using the MEGAscript T7 transcription kit (Ambion) in the presence of 250 nM Cy 3- or Cy 5-UTP for fluorescently labeled RNAs. mCh-tagged protein-coding mRNAs were generated using the mMessage machine transcription kit (Ambion) from linearized plasmids, as follows: pSP64:mCh-hnRNPABx2, pSP64:Stau1-mCh, pSP64:Vera-mCh, and pSP64:YBX1-mCh. Cy-labeled RNAs were injected at 200 nM, mCh RNAs were injected at 500 nM, and barcoded RNAs were injected at 1.25 nM. Following microinjection, oocytes were cultured for 16–24 h at 18°C in XOCM.

FISH and IF

Oocytes were fixed for 1 h at 22°C in FTG (80 mM K PIPES, pH 6.8, 1 mM $MgCl_2$, 5 mM EGTA, 0.2% Triton X-100, 3.7% formaldehyde, 0.25% glutaraldehyde, 0.5 µm paclitaxel), followed by postfixation in 100% methanol overnight at 22°C (Becker and Gard, 2006). After rehydration in Tris-buffered saline (TBS), oocytes were incubated overnight at 4°C in 100 mM $NaBH_4$ in TBS (Becker and Gard, 2006). After two washes in TBSN (0.1% NP-40 in TBS), followed by two washes in TBSNB (0.2% ultrapure bovine serum albumin [BSA] in TBSN), oocytes were equilibrated stepwise in TBSNB-30S

(30% sucrose in TBSNB) and, after equilibration in an embedding mold, TBSNB-30S was replaced with OCT compound and snap-frozen in an ethanol–dry ice bath.

Cryosectioning and FISH was performed as described in Neil and Mowry (2018), with custom Stellaris FISH probes (LGC Biosearch Technology) for *gapdh*, *trim36*, *vegT*, and *vg1* applied at 500 nM. To avoid detection of injected *LE* RNA, a modified *vg1*ΔLE probe set was engineered to exclude nts. 1378–1715, which correspond to the *vg1 LE* sequence. For combined FISH-IF, slides were subsequently washed twice in TBSNB, incubated for 3 h at 22°C in TBS-plus (5% vol/vol normal goat serum, 2 mg/ml ultrapure BSA in TBSN), and incubated overnight at 4°C with primary antibodies at 20 µg/ml in TBS-plus. Primary antibodies (Supplemental Table S10) were directly labeled with Alexa-405, Alexa-546, or Alexa-647 using Zenon labeling kits (ThermoFisher). After four 10-min washes in TBSNB at 22°C, slides were mounted with ProLong Gold Antifade. For thioflavin staining, cryosections were incubated in thioflavin S solution (Sigma; 1% in 80% ethanol) for 20 min, at room temperature, followed by washes with 80% ethanol, 70% ethanol, and H_2O. Slides were either mounted in Prolong Gold Antifade or processed for FISH as described previously (Neil and Mowry, 2018), with probe sets restricted to Quasar 670 to avoid overlap with the thioflavin fluorescence. Care was taken with image acquisition due to the lower quantum yield for thioflavion compared with the other fluorophores used. Images were acquired at room temperature on a Zeiss LSM 800 confocal laser scanning microscope with GaAsP detectors using plan apochromat 20× water and 63× oil objectives (NA = 0.8 and 1.4, respectively). Images were acquired, and image tiles were stitched with Zen software. Further image processing was performed in ImageJ software; the point squared function was calculated by the "Defraction PSF" plugin, and deconvolution was carried out with the "Iterative Deconvolve 3D" plugin.

Oocyte lysate preparation

Approximately 2500 stage II–III oocytes were washed with phosphate-buffered saline (PBS), followed by cross-linking (0.1% formaldehyde in PBS) for 10 min at 22°C. The reaction was quenched with 0.25 M glycine (in 25 mM Tris pH 7.4,) for 5 min at 22°C. Oocytes were washed in column running buffer (CRB): 0.05% NP-40, 1 mM DTT, 10 mM HEPES, pH 7.4, 100 mM KOAc, 3 mM MgOAc, 5 mM EGTA, 100 mM sucrose, 2 nU/ml Ribolock RNase Inhibitor (Life Technologies), and 1× HALT Protease Inhibitors (ThermoFisher). After homogenizing in CRB (~20 oocytes/µl), the lysate was clarified by centrifugation at 10,000 × *g* for 10 min at 4°C and adjusted to a final protein concentration of 50 mg/ml in CRB.

Size exclusion (SE) chromatography

Oocyte lysate was chromatographed on Sephacryl S400 HR resin (GE Healthcare) in CRB. Column fractions were analyzed by RT-qPCR for *vg1* mRNA and by immunoblot for proteins of interest. Fractions containing the *vg1* RNA peak were pooled for mass spec and RNA-seq analyses. RNA was isolated using the Direct-Zol RNA MicroPrep kit (Genesee), and cDNA was prepared using the iScript cDNA synthesis kit (Bio-Rad). To control for RNA extraction efficiency, 2.5 pg of *luciferase* (*luc*) RNA (Promega) was added to each column fraction as an exogenous reference RNA (Johnston *et al.*, 2012). For analysis of *vg1* mRNA distribution across fractions, RT-qPCR was performed using Luna One-Step qPCR (New England Biolabs) with forward (qPCR vg1 Fwd) and reverse (qPCR vg1 Rev) *vg1* primers and forward (qPCR luc Fwd) and reverse (qPCR luc Rev) *luc* primers (Supplemental Table S9). For RNase treatment of oocyte lysates prior to SE chromatography, Ribolock RNase Inhibitor was omitted from all buffers, and RNase A was added to a final concentration of 0.1 µg/µl and incubated for 10 min at 37°C.

IP and immunoblotting

For MS and RNA-seq analyses, anti-hnRNPAB, anti-Stau1, and IgG were covalently cross-linked to Dynabeads (Invitrogen), which were washed in 0.1% BSA for 5 min at 22°C, blocked for 1 h in RNA blocking solution (0.05% CHAPS, 0.32 µg/µl torula RNA, PBS), and washed three times in CRB. SE *vg1* RNA peak "pool" was incubated for 6 h at 4°C with antibody-coupled Dynabeads in PIP buffer (50 mM Tris, pH 7.4, 0.1% NP40, 0.05 mM $MgCl_2$, 2 nU/ml Ribolock RNase Inhibitor, and 1× HALT Protease Inhibitors) for protein co-IP, or in RIP buffer (25 mM Tris, pH 7.4, 0.5% NP40, 0.5 mM DTT, 150 mM KCl, 5 mM EDTA, 2 nU/ml Ribolock RNase Inhibitor, 1× HALT Protease Inhibitors) for RNA co-IP. For RNA-seq analysis, RNA was extracted using Trizol (Invitrogen). For MS, bound proteins were eluted with 50 mM Tris, pH 8.0, 0.2% SDS, and 0.1% Tween-20 at 25°C, followed by incubation at 70°C for 1 h to reverse the cross-linking and removal of Tween-20 using HiPPR columns (ThermoFisher). For immunoblotting, antibodies (Supplemental Table S10) were used at 1:1000, except for PTB (1:2000), Stau1 (1:2000), Tubulin (1:500), Vera (1:2000), and Ybx1 (1:100). Secondary antibodies (goat anti-rabbit IgG or goat anti-mouse IgG) were used at 1:10,000. For RNA-IPs, two step RT-qPCR was performed using SybrGreen Powerup MasterMix (ABI).

MS

LC-MS/MS was performed at the COBRE CCRD Proteomics Core Facility (RI Hospital) on an automated platform (Yu *et al.*, 2009; Yu and Salomon, 2010) connected to a Q Exactive Plus mass spectrometer (ThermoFisher Scientific) as detailed in Ahsan *et al.* (2017). Peptide spectrum matching (PSM) of MS/MS spectra of each file was searched against a species-specific database (*X. laevis;* UniProt) using MASCOT v. 2.4 (Matrix Science). A concatenated database containing "target" and "decoy" sequences was employed to estimate the false discovery rate (FDR) (Elias and Gygi, 2007). Msconvert v. 3.0.5047 (ProteoWizard), using default parameters and with the MS2Deisotope filter on, was employed to create peak lists for Mascot. The Mascot database search was performed with the following parameters: trypsin enzyme cleavage specificity, two possible missed cleavages, 10 ppm mass tolerance for precursor ions, 20 mmu mass tolerance for fragment ions. Search parameters permitted variable modification of methionine oxidation (+15.9949 Da) and static modification of carbamidomethylation (+57.0215 Da) on cysteine. The resulting PSMs were reduced to sets of unique PSMs by eliminating lower scoring duplicates. To provide high confidence, the Mascot results were filtered for Mowse Score (>20). Peptide assignments from the database search were filtered down to a 1% FDR by a logistic spectral score as previously described (Elias and Gygi, 2007; Yu *et al.*, 2009). Downstream analysis was performed in-house using R/R Studio (v3.5.0/v1.1.447 and v1.1.453). For Stau1 and hnRNPAB IPs, only those proteins containing peptides in at least three biological replicates were considered. Enrichment over IgG was determined if the sum of peptides across all four biological replicates was as least twofold greater than the sum of the peptides in all four IgG experiments. For unannotated protein hits (i.e., LOC, MGC, Xelaev, Xetrov delimitators), peptides were BLAST against the *X. laevis* JGI 9.1v1.8.3.2 annotation database, available from xenbase.org.

RNA-seq analysis

After depletion of rRNA using the RiboZero kit (Illumina) libraries were prepared using the Illumina TruSeq RNA-seq kit (Illumina).

Sequencing of the libraries was performed by Genewiz using Illumina 150-bp paired-end sequencing on an Illumina HiSeq2500. Sequencing data and derived files were deposited to the NCBI GEO repository. High-quality-run data were first confirmed by FastQC (Andrews, 2010) and then preprocessed to trim adapters, remove PhiX spike-in control, and remove rRNA contamination. Read trimming was determined to not significantly improve the quality of the raw data. The data were first aligned against NCBI *X. laevis* genome version 9.2 using STAR (version 2.6.1b; Dobin *et al.*, 2013; Kwon, 2015), with a genome .fasta file and .gtf file downloaded from xenbase.org (XENLA_9.2_genome.fa and XENLA_9.2_Xenbase.gtf, respectively; Karimi *et al.*, 2018). Raw transcript counts from the aligned data were then quantitated using HTseq (version 0.9.1; Anders *et al.*, 2015), specifically, the htseq-count command referenced against the same .gtf file. Differential expression analysis was done using EdgeR (version 3.12; Robinson *et al.*, 2010), and gene names were identified using the XENLA_9.2_Xenbase.transcripts.fa file from Xenbase. Unannotated gene names (i.e., LOC, MGC, Xelaev delimitators) were searched on NCBI Gene for identification and replaced where possible. Lists of enriched transcripts were generated using EdgeR, comparing the RNAs immunoprecipitated by Stau1, hnRNPAB, and IgG. The final list was then generated by filtering for RNAs that were at least 1.8-fold enriched in both the Stau1 and the hnRNPAB RIPs compared with IgG, with a q value of < 0.05. For validation, RNA was isolated from the *vg1* RNA peak pool (LB) and Tubulin peak pool (non-LB) fractions after SE chromatography. Briefly, 2.5 pg of *luciferase* RNA (Promega #L4561) were applied to samples just prior to RNA extraction which was performed using TriZol (Invitrogen) based on the manufacturer's instructions. cDNA was prepared using the iScript cDNA synthesis kit (Bio-Rad, #1708891) as per manufacturer's protocols. Using primers listed in Supplemental Table S9, RT-qPCR was performed with PowerUp SYBR green master mix (ABI), and gene expression was normalized to *luciferase* with the Pfaffl method (Pfaffl, 2001), an assumption-free version of the ΔΔC method (Livak and Schmittgen, 2001).

GO, domain, and motif analyses

GO analysis was determined using DAVID (Huang *et al.*, 2009a, b), with *Xenopus tropicalis* as background. Identification of putative IDRs were determined using SLIDER (Peng *et al.*, 2014), which predicts long disordered segments (>30 consecutive disordered residues), against the hnRNPAB/Stau1 proteomic dataset or the *X. laevis* J-strain 9.2 genome (xenbase.org). Only those proteins with a SLIDER score greater than 0.55 were considered likely to have an IDR. Prionlike domains were calculated using PLAAC (Lancaster *et al.*, 2014) with default settings. Only those proteins with a CORE-score greater than zero were considered to have a prionlike domain. Motif analysis for the L-body RNA pool was done using MEME (Bailey and Elkan, 1994) using a stranded analysis and a maximum motif length of 10.

FRAP

Two nl of RNA encoding mCh-tagged proteins (at 500 nM) or fluorescently labeled RNAs (at 200 nM) were injected into stage II oocytes and allowed to localize for 48 h in XOCM for 18°C. Oocytes were imaged live in XOCM at room temperature on an Olympus FV3000 confocal microscope with a UPLSAPO 30× silicon oil UPlan Super Apochromat objective (NA = 1.05). A 10-μm^2 ROI was bleached using a 561-nm laser at 100% for 2 s. Recovery was monitored at 5-s intervals for 100 iterations. FRAP calculations were as previously described (Gagnon *et al.*, 2013) and curve fitting was performed in GraphPad Prism 8 using Y = Y0 + (Plateau-Y0)*(1-exp(-K*x).

Quantification and statistical analysis

All bioinformatics analysis was carried out with either R/R Studio (v3.5.0/v1.1.447 or v1.1.453) or Microsoft Excel (Office 365) software. For RNA-IP analysis, LinRegPCR (Ramakers *et al.*, 2003) was used to calculate primer efficiency for both *vg1* and *luciferase* primers. The geometric mean of primer efficiency was calculated in Excel for each primer across four experimental replicates. The relative fold enrichment was calculated using the Pfaffl method (Pfaffl, 2001) and the geometric mean efficiency of *vg1* and *luciferase* primers as determined by LinRegPCR (Ramakers *et al.*, 2003). Log2 fold enrichment of *vg1* in RBP-IPs was calculated relative to IgG and normalized to *luciferase*. Four replicates were performed, and a Mann–Whitney U test was performed for statistical significance (De Neve *et al.*, 2013) using R studio. Statistics relating to relative enrichment of GO annotations, intrinsically disordered domains, and prionlike domains were performed in R/R studio (v3.5.0/v1.1.453) using the Fisher's exact test.

Data availability

MS proteomics data have been deposited to the ProteomeXchange Consortium via the PRIDE (Perez-Riverol *et al.*, 2019) protein repository with the dataset identifier PXD013742. The RNA-seq data have been deposited to NCBI GEO repository (#GSE158246), available at https://www.ncbi.nlm.nih.gov/geo/query/acc.cgi?acc=GSE158246.

ACKNOWLEDGMENTS

We thank J. Fallon, N. Fawzi and E. Larschan, for comments on the manuscript. This work was funded by grant R01-GM071049 from the NIH to KLM. CRN, SPJ, and LCO were supported in part by NIH grant T32-GM07601. Mass spectrometry was performed in the Rhode Island Hospital, COBRE CCRD Proteomics Core Facility (supported by P30-GM110759) with advice and technical support from A.R. Salomon and N. Ahsan.

REFERENCES

Ahsan N, Belmont J, Chen Z, Clifton JG, Salomon AR (2017). Highly reproducible improved label-free quantitative analysis of cellular phosphoproteome by optimization of LC-MS/MS gradient and analytical column construction. J Proteomics 165, 69–74.

Alberti S, Hyman AA (2016). Are aberrant phase transitions a driver of cellular aging? BioEssays 38, 959–968.

Allison R, Czaplinski K, Git A, Adegbenro E, Stennard F, Houliston E, Standart N (2004). Two distinct Staufen isoforms in Xenopus are vegetally localized during oogenesis. RNA 10, 1751–1763.

Anders S, Pyl PT, Huber W (2015). HTSeq–a Python framework to work with high-throughput sequencing data. Bioinformatics 31, 166–169.

Andrews S (2010). FASTQC. A quality control tool for high throughput sequence.

Arthur PK, Claussen M, Koch S, Tarbashevich K, Jahn O, Pieler T (2009). Participation of Xenopus Elr-type proteins in vegetal mRNA localization during oogenesis. J Biol Chem 284, 19982–19992.

Bailey TL, Elkan C (1994). Fitting a mixture model by expectation maximization to discover motifs in biopolymers. Proceedings Int Conf Intell Syst Mol Biol 2, 28–36.

Banani SF, Lee HO, Hyman AA, Rosen MK (2017). Biomolecular condensates: Organizers of cellular biochemistry. Nat Rev Mol Cell Biol 18, 285–298..

Batish M, van den Bogaard P, Kramer FR, Tyagi S (2012). Neuronal mRNAs travel singly into dendrites. Proc Natl Acad Sci USA 109, 4645–4650.

Becker BE, Gard DL (2006). Visualization of the cytoskeleton in Xenopus oocytes and eggs by confocal immunofluorescence microscopy. Methods Mol Biol 322, 69–86.

Betley JN, Heinrich B, Vernos I, Sardet C, Prodon F, Deshler JO (2004). Kinesin II mediates Vg1 mRNA transport in Xenopus oocytes. Curr Biol 14, 219–224.

Boeynaems S, Alberti S, Fawzi NL, Mittag T, Polymenidou M, Rousseau F, Schymkowitz J, Shorter J, Wolozin B, Van Den Bosch L, *et al.* (2018). Protein phase separation: A new phase in cell biology. Trends Cell Biol 28, 420–435.

Boke E, Ruer M, Wühr M, Coughlin M, Lemaitre R, Gygi SP, Alberti S, Drechsel D, Hyman AA, Mitchison TJ (2016). Amyloid-like self-assembly of a cellular compartment. Cell 166, 637–650.
Bubunenko M, Kress TL, Vempati UD, Mowry KL, King ML (2002). A consensus RNA signal that directs germ layer determinants to the vegetal cortex of Xenopus oocytes. Dev Biol 248, 82–92.
Buchan JR (2014). mRNP granules assembly, function, and connections with disease. RNA Biol 11, 1019–1030.
Burke JM, Lester ET, Tauber D, Parker R (2020). RNase L promotes the formation of unique ribonucleoprotein granules distinct from stress granules. J Biol Chem 295, 1426–1438.
Buxbaum AR, Wu B, Singer RH (2014). Single -actin mRNA detection in neurons reveals a mechanism for regulating its translatability. Science (80-) 343, 419–422.
Colegrove-Otero LJ, Devaux A, Standart N (2005). The Xenopus ELAV protein ElrB represses Vg1 mRNA translation during oogenesis. Mol Cell Biol 25, 9028–9039.
Cote CA, Gautreau D, Denegre JM, Kress TL, Terry NA, Mowry KL (1999). A Xenopus protein related to hnRNP I has a role in cytoplasmic RNA localization. Mol Cell 4, 431–437.
Czaplinski K, Kocher T, Schelder M, Segref A, Wilm M, Mattaj IW (2005). Identification of 40LoVe, a Xenopus hnRNP D family protein involved in localizing a TGF-beta-related mRNA during oogenesis. Dev Cell 8, 505–515.
Czaplinski K, Mattaj IW (2006). 40LoVe interacts with Vg1RBP/Vera and hnRNP I in binding the Vg1-localization element. RNA 12, 213–222.
Deshler JO, Highett MI, Abramson T, Schnapp BJ (1998). A highly conserved RNA-binding protein for cytoplasmic mRNA localization in vertebrates. Curr Biol 8, 489–496.
Dobin A, Davis CA, Schlesinger F, Drenkow J, Zaleski C, Jha S, Batut P, Chaisson M, Gingeras TR (2013). STAR: ultrafast universal RNA-seq aligner. Bioinformatics 29, 15–21.
Dodson AE, Kennedy S (2020). Phase separation in germ cells and development. Dev Cell 55, 4–17.
Elbaum-Garfinkle S, Kim Y, Szczepaniak K, Chen CCH, Eckmann CR, Myong S, Brangwynne CP (2015). The disordered P granule protein LAF-1 drives phase separation into droplets with tunable viscosity and dynamics. Proc Natl Acad Sci USA 112, 7189–7194.
Elias JE, Gygi SP (2007). Target-decoy search strategy for increased confidence in large-scale protein identifications by mass spectrometry. Nat Methods 4, 207–214.
Ferrandon D, Koch I, Westhof E, Nusslein-Volhard C (1997). RNA-RNA interaction is required for the formation of specific bicoid mRNA 3' UTR-STAUFEN ribonucleoprotein particles. EMBO J 16, 1751–1758.
Gagnon JA, Kreiling JA, Powrie EA, Wood TR, Mowry KL (2013). Directional transport Is mediated by a dynein-dependent step in an RNA localization pathway. PLoS Biol 11. doi:10.1371/journal.pbio.1001551.
Gautreau D, Cote CA, Mowry KL (1997). Two copies of a subelement from the Vg1 RNA localization sequence are sufficient to direct vegetal localization in Xenopus oocytes. Development 124, 5014–5020.
Gilman B, Tijerina P, Russell R (2017). Distinct RNA-unwinding mechanisms of DEAD-box and DEAH-box RNA helicase proteins in remodeling structured RNAs and RNPs. Biochem Soc Trans 45, 1313–1321.
Gomes E, Shorter J (2019). The molecular language of membraneless organelles. J Biol Chem 294, 7115–7127.
Guntern R, Bouras C, Hof PR, Vallet PG (1992). An improved thioflavine S method for staining neurofibrillary tangles and senile plaques in Alzheimer's disease. Experientia 48, 8–10.
Han B, Antkowiak KR, Fan X, Rutigliano M, Ryder SP, Griffin EE (2018). Polo-like kinase couples cytoplasmic protein gradients in the C. elegans zygote. Curr Biol 28, 60–69.e8.
Han TW, Kato M, Xie S, Wu LC, Mirzaei H, Pei J, Chen M, Xie Y, Allen J, Xiao G, McKnight SL (2012). Cell-free formation of RNA granules: Bound RNAs identify features and components of cellular assemblies. Cell 149, 768–779.
Havin L, Git A, Elisha Z, Oberman F, Yaniv K, Schwartz SP, Standart N, Yisraeli JK (1998). RNA-binding protein conserved in both microtubule- and microfilament- based RNA localization. Genes Dev 12, 1593–1598.
Heasman J, Wessely O, Langland R, Craig EJ, Kessler DS (2001). Vegetal localization of maternal mRNAs is disrupted by VegT depletion. Dev Biol 240, 377–386.
Heraud-Farlow JE, Kiebler MA (2014). The multifunctional Staufen proteins: conserved roles from neurogenesis to synaptic plasticity. Trends Neurosci 37, 470–479.
Holt CE, Martin KC, Schuman EM (2019). Local translation in neurons: visualization and function. Nat Struct Mol Biol 26, 557–566.
Huang DW, Sherman BT, Lempicki RA (2009a). Bioinformatics enrichment tools: paths toward the comprehensive functional analysis of large gene lists. Nucleic Acids Res 37, 1–13.
Huang DW, Sherman BT, Lempicki RA (2009b). Systematic and integrative analysis of large gene lists using DAVID bioinformatics resources. Nat Protoc 4, 44–57.
Hubstenberger A, Noble SL, Cameron C, Evans TC (2013). Translation repressors, an RNA helicase, and developmental cues control RNP phase transitions during early development. Dev Cell 27, 161–173.
Jain A, Vale RD (2017). RNA phase transitions in repeat expansion disorders. Nature 546, 243–247.
Jain S, Wheeler JR, Walters RW, Agrawal A, Barsic A, Parker R (2016). ATPase-modulated stress granules contain a diverse proteome and substructure. Cell 164, 487–498.
Jambor H, Brunel C, Ephrussi A (2011). Dimerization of oskar 3' UTRs promotes hitchhiking for RNA localization in the Drosophila oocyte. RNA 17, 2049–2057.
Johnston S, Gallaher Z, Czaja K (2012). Exogenous reference gene normalization for real-time reverse transcription-polymerase chain reaction analysis under dynamic endogenous transcription. Neural Regen Res 7, 1064–1072.
Karimi K, Fortriede JD, Lotay VS, Burns KA, Wang DZ, Fisher ME, Pells TJ, James-Zorn C, Wang Y, Ponferrada VG, *et al.* (2018). Xenbase: a genomic, epigenomic and transcriptomic model organism database. Nucleic Acids Res 46, D861–D868.
Kato M, Han TW, Xie S, Shi K, Du X, Wu LC, Mirzaei H, Goldsmith EJ, Longgood J, Pei J, *et al.* (2012). Cell-free formation of RNA granules: Low complexity sequence domains form dynamic fibers within hydrogels. Cell 149, 753–767.
Kedersha N, Ivanov P, Anderson P (2013). Stress granules and cell signaling: More than just a passing phase? Trends Biochem Sci 38, 494–506.
Kloc M, Wilk K, Vargas D, Shirato Y, Bilinski S, Etkin LD (2005). Potential structural role of non-coding and coding RNAs in the organization of the cytoskeleton at the vegetal cortex of Xenopus oocytes. Development 132, 3445–3457.
Krieg PA, Melton DA (1984). Functional messenger RNAs are produced by SP6 in vitro transcription of cloned cDNAs. Nucleic Acids Res 12, 7057–7070.
Kwon T (2015). Benchmarking transcriptome quantification methods for duplicated genes in Xenopus laevis. Cytogenet Genome Res 145, 253–264.
Lancaster AK, Nutter-Upham A, Lindquist S, King OD (2014). PLAAC: a web and command-line application to identify proteins with prion-like amino acid composition. Bioinformatics 30, 2501–2502.
Langdon EM, Qiu Y, Niaki AG, Mclaughlin GA, Weidmann CA, Gerbich TM, Smith JA, Crutchley JM, Termini CM, Weeks KM, *et al.* (2018). mRNA structure determines specificity ofa polyQ-driven phase separation. Science (80-) 360, 922–927.
Lewis RA, Gagnon JA, Mowry KL (2008). PTB/hnRNP I is required for RNP remodeling during RNA localization in Xenopus oocytes. Mol Cell Biol 28, 678–686.
Li P, Banjade S, Cheng H-CC, Kim S, Chen B, Guo L, Llaguno M, Hollingsworth JV, King DS, Banani SF, *et al.* (2012). Phase transitions in the assembly of multivalent signalling proteins. Nature 483, 336–340.
Lin Y, Protter DSW, Rosen MK, Parker R (2015). Formation and maturation of phase-separated liquid droplets by RNA-binding proteins. Mol Cell 60, 208–219.
Little SC, Sinsimer KS, Lee JJ, Wieschaus EF, Gavis ER (2015). Independent and coordinate trafficking of single Drosophila germ plasm mRNAs. Nat Cell Biol 17, 558–568.
Liu X, Morency E, Li T, Qin H, Zhang X, Zhang X, Coonrod S (2017). Role for PADI6 in securing the mRNA-MSY2 complex to the oocyte cytoplasmic lattices. Cell Cycle 16, 360–366.
Livak KJ, Schmittgen TD (2001). Analysis of relative gene expression data using real-time quantitative PCR and the 2(-Delta Delta C(T)) Method. Methods 25, 402–408.
Messitt TJ, Gagnon JA, Kreiling JA, Pratt CA, Yoon YJ, Mowry KL (2008). Multiple kinesin motors coordinate cytoplasmic RNA transport on a subpopulation of microtubules in Xenopus oocytes. Dev Cell 15, 426–436.
Mili S, Steitz JA (2004). Evidence for reassociation of RNA-binding proteins after cell lysis: implications for the interpretation of immunoprecipitation analyses. RNA 10, 1692–1694.
Mittag T, Parker R (2018). Multiple modes of protein–protein interactions promote RNP granule assembly. J Mol Biol 430, 4636–4649.
Miura K, Rueden C, Hiner M, Schindelin J, Rietdorf J (2014). ImagJ plugin CorrectBleach V2.0.2. doi:10.5281/zenodo.30769.

Neil CR, Mowry K (2018). Fluorescence in situ hybridization of cryosectioned Xenopus oocytes. Cold Spring Harb Protoc 2018, pdb.prot097030. doi:10.1101/pdb.prot097030.
De Neve J, Thas O, Ottoy JP, Clement L (2013). An extension of the Wilcoxon-Mann-Whitney test for analyzing RT-qPCR data. Stat Appl Genet Mol Biol 12, 333–346.
Niepielko MG, Eagle WVI, Gavis ER (2018). Stochastic seeding coupled with mRNA self-recruitment generates heterogeneous Drosophila germ granules. Curr Biol 28, 1872–1881.e3.
Nilsson MR (2004). Techniques to study amyloid fibril formation in vitro. Methods 34, 151–160.
Nott TJ, Petsalaki E, Farber P, Jervis D, Fussner E, Plochowietz A, Craggs TD, Bazett-Jones DP, Pawson T, Forman-Kay JD, Baldwin AJ (2015). Phase transition of a disordered nuage protein generates environmentally responsive membraneless organelles. Mol Cell 57, 936–947.
Oh D, Houston DW (2017). RNA localization in the lertebrate oocyte: Establishment of oocyte polarity and localized mRNA assemblages. Results Probl Cell Differ 63, 189–208.
Peng Z, Mizianty MJ, Kurgan L (2014). Genome-scale prediction of proteins with long intrinsically disordered regions. Proteins Struct Funct Bioinforma 82, 145–158.
Perez-Riverol Y, Csordas A, Bai J, Bernal-Llinares M, Hewapathirana S, Kundu DJ, Inuganti A, Griss J, Mayer G, Eisenacher M, *et al*. (2019). The PRIDE database and related tools and resources in 2019: improving support for quantification data. Nucleic Acids Res 47, D442–D450.
Pfaffl MW (2001). A new mathematical model for relative quantification in real-time RT-PCR. Nucleic Acids Res 29, e45.
Protter DSW, Rao BS, Van Treeck B, Lin Y, Mizoue L, Rosen MK, Parker R (2018). Intrinsically disordered regions can contribute promiscuous interactions to RNP granule assembly. Cell Rep 22, 1401–1412.
Putnam A, Cassani M, Smith J, Seydoux G (2019). A gel phase promotes condensation of liquid P granules in Caenorhabditis elegans embryos. Nat Struct Mol Biol 26. doi:10.1038/s41594-019-0193-2.
Ramakers C, Ruijter JM, Deprez RHL, Moorman AFM (2003). Assumption-free analysis of quantitative real-time polymerase chain reaction (PCR) data. Neurosci Lett 339, 62–66.
Robinson MD, McCarthy DJ, Smyth GK (2010). edgeR: a Bioconductor package for differential expression analysis of digital gene expression data. Bioinformatics 26, 139–140.
Ryder PV, Lerit DA (2018). RNA localization regulates diverse and dynamic cellular processes. Traffic 19, 496–502.
Shin Y, Brangwynne CP (2017). Liquid phase condensation in cell physiology and disease. Science 357. doi:10.1126/science.aaf4382.
Snedden DD, Bertke MM, Vernon D, Huber PW (2013). RNA localization in Xenopus oocytes uses a core group of trans-acting factors irrespective of destination. RNA 19, 889–895.
Suter B (2018). RNA localization and transport. Biochim Biophys Acta Gene Regul Mech 1861, 938–951.
Tafuri SR, Wolffe AP (1990). Xenopus Y-box transcription factors: molecular cloning, functional analysis and developmental regulation. Proc Natl Acad Sci USA 87, 9028–9032.
Tauber D, Tauber G, Khong A, Van Treeck B, Pelletier J, Parker R (2020). Modulation of RNA condensation by the DEAD-Box protein eIF4A. Cell 180, 411–426.e16.
Trcek T, Douglas TE, Grosch M, Yin Y, Eagle WVI, Gavis ER, Shroff H, Rothenberg E, Lehmann R (2020). Sequence-independent self-assembly of germ granule mRNAs into homotypic clusters. Mol Cell 78, 941-950.e12.
Van Treeck B, Protter DSW, Matheny T, Khong A, Link CD, Parker R (2018). RNA self-assembly contributes to stress granule formation and defining the stress granule transcriptome. Proc Natl Acad Sci USA 115, 2734–2739.
Uversky VN (2017). Intrinsically disordered proteins in overcrowded milieu: Membraneless organelles, phase separation, and intrinsic disorder. Curr Opin Struct Biol 44, 18–30.
Wang JT, Smith J, Chen BC, Schmidt H, Rasoloson D, Paix A, Lambrus BG, Calidas D, Betzig E, Seydoux G (2014). Regulation of RNA granule dynamics by phosphorylation of serine-rich, intrinsically disordered proteins in C. elegans. Elife 3, e04591.
Weeks DL, Melton DA (1987). A maternal mRNA localized to the vegetal hemisphere in Xenopus eggs codes for a growth factor related to TGF-beta. Cell 51, 861–867.
Xu S, Li Q, Xiang J, Yang Q, Sun H, Guan A, Wang L, Liu Y, Yu L, Shi Y, *et al*. (2016). Thioflavin T as an efficient fluorescence sensor for selective recognition of RNA G-quadruplexes. Sci Rep 6, 24793.
Yisraeli JK (2005). VICKZ proteins: a multi-talented family of regulatory RNA-binding proteins. Biol Cell 97, 87–96.
Yoon YJ, Mowry KL (2004). Xenopus Staufen is a component of a ribonucleoprotein complex containing Vg1 RNA and kinesin. Development 131, 3035–3045.
Yu K, Sabelli A, DeKeukelaere L, Park R, Sindi S, Gatsonis CA, Salomon A (2009). Integrated platform for manual and high-throughput statistical validation of tandem mass spectra. Proteomics 9, 3115–3125.
Yu K, Salomon AR (2010). HTAPP: A high-throughput autonomous proteomic pipeline. Proteomics 10, 2113–2122.
Zhang J, King ML (1996). Xenopus VegT RNA is localized to the vegetal cortex during oogenesis and encodes a novel T-box transcription factor involved in mesodermal patterning. Development 122, 4119–4129.